
Multi-Material Topology Optimization with
Continuous Magnetization Direction for Permanent
Magnet Synchronous Reluctance Motors

T. Gauthey, P. Gangl, M. Hage Hassan

**Berichte aus dem
Institut für Angewandte Mathematik**

Technische Universität Graz

Multi-Material Topology Optimization with Continuous Magnetization Direction for Permanent Magnet Synchronous Reluctance Motors

T. Gauthey, P. Gangl, M. Hage Hassan

**Berichte aus dem
Institut für Angewandte Mathematik**

Bericht 2021/12

Technische Universität Graz
Institut für Angewandte Mathematik
Steyrergasse 30
A 8010 Graz

WWW: <http://www.applied.math.tugraz.at>

© Alle Rechte vorbehalten. Nachdruck nur mit Genehmigung des Autors.

Multi-Material Topology Optimization with Continuous Magnetization Direction for Permanent Magnet Synchronous Reluctance Motors

Thomas Gauthey^{*1,2}, Peter Gangl^{†2}, and Maya Hage Hassan^{‡1}

¹ Université Paris-Saclay, CentraleSupélec, CNRS, Laboratoire de Génie Electrique et Electronique de Paris, 91192, Gif-sur-Yvette, France. ,
Sorbonne Université, CNRS, Laboratoire de Génie Electrique et Electronique de Paris, 75252, Paris, France.

²Technische Universität Graz, Institut für Angewandte Mathematik, 8010 Graz, Austria.

July 10, 2021

Abstract

Permanent magnet-assisted synchronous reluctance motors (PMSynRM) have a significantly higher average torque than synchronous reluctance motors. Thus, determining an optimal design results in a multi-material topology optimization problem, where one seeks to distribute ferromagnetic material, air and permanent magnets within the rotor in an optimal manner. This study proposed a novel density-based distribution scheme, which allows for continuous magnetization direction instead of a finite set of angles. Thus, an interpolation scheme is established between properties pertaining to magnets and non-linear materials. This allows for new designs to emerge without introducing complex geometric parameterization or relying on the user's biases and intuitions. Toward reducing computation time, Nitsche-type mortaring is applied, allowing for free rotation of the rotor mesh relative to the stator mesh. The average torque is approximated using only four-point static positions. This study investigates several interpolation schemes and presents a new one inspired by the topological derivative. We propose to filter the final design for the magnetization angle using K-mean clustering accounting for technical feasibility constraints of magnets. Finally, the design of the electrical motor is proposed to maximize torque value.

Keywords: Topology optimization, Permanent magnets machines, Design optimization, Acceleration methods

^{*}E-Mail: thomas.gauthey(at)geeps.centralesupelec.fr

[†]E-Mail: gangl(at)math.tugraz.at

[‡]E-Mail: maya.hage-hassan(at)centralesupelec.fr

1 Introduction

Synchronous reluctance machines (SynRM) are standard in households and industrial applications, thanks to their cheap cost compared to permanent magnet motors and advances in manufacturing techniques. Although the deployment of these machines continues [15], PMSynRM offers an excellent alternative for both structures, solving for SynRM, its poor power factor and, for permanent magnet machines (PMM), its cost. The design of these machines using parametric optimization often necessitates either complex analytical models or the use of Finite Element Analysis (FEA) relying heavily on experienced engineers and known good designs [23].

Density based optimizations allow for bypassing such cumbersome frameworks. Although they were first developed for two materials application in continuous mechanics [33], a rise in n-materials optimization in the field of electromagnetics has allowed for new PMM and SynRM to emerge [14, 18]. In most optimizations where permanent magnets are involved, magnetization direction are fixed [29] or limited to a set of a couple values [6, 7, 20]. If continuous directions are considered during the optimization process, the final design is filtered to take into account only a couple of predefined directions to meet manufacturing constraints [17, 36].

In this paper we propose a simultaneous density-based optimization scheme consisting of three-material (air-iron-magnet) with a continuous magnetization direction. The proposition is applied to design the rotor of a distributed winding stator as described in [11, 25] to maximize the mean torque under constraints. The final designs are filtered using an unbiased K-means heuristic for accounting

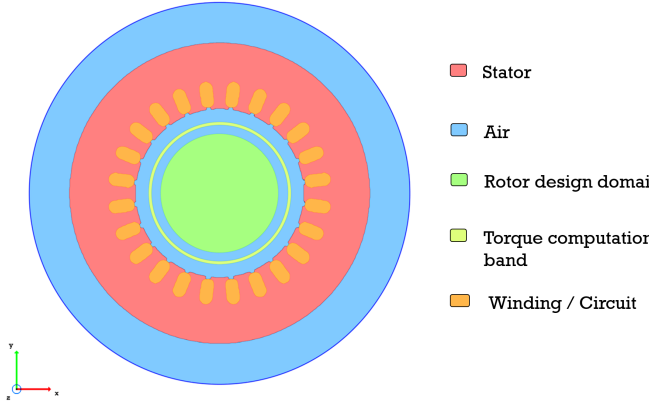


Figure 1: Machine geometry

Table 1: Geometric parameters

Parameter	Value
Slot number	24
Axial length	50.0 mm
Outer rotor radius	18.5 mm
Inner stator radius	26.5 mm
Outer stator radius	47.5 mm
Air gap length	8.0 mm

for feasibility constraints. Here, we propose also to accelerate the torque calculation through a four-point method.

2 Problem description

We chose to investigate a SynRM described in [11, 25], of which the rotor design had proven to be a challenging problem for topology optimization and use it for our PM-SynRM optimization problem.

2.1 Geometry description

The electrical machine geometry and current density distributions are given respectively in Figure 1 and 2. The dimensions for the considered machine are given in Table 1.

This machine differs from most conventional SynRM by its large air gap which constrains the statoric winding distribution to only one pair of poles (cf. Figure 2).

We introduce the relationship between the electrical angle θ_{elec} and the mechanical angle θ

$$\theta_{elec} = n_{pp} \theta, \quad (2.1)$$

with n_{pp} the number of pair of poles, here $n_{pp} = 1$.

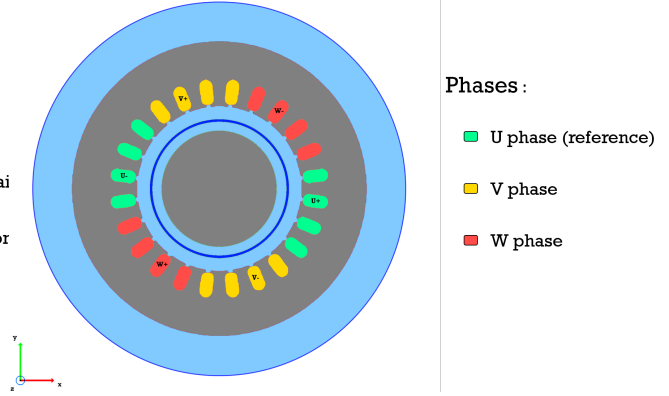


Figure 2: Statoric winding distribution and current parameters

Table 2: Statoric winding parameters

Parameter	Value
Number of turn N_s	64
Winding type	Distributed
Connection type	Star
Resistance ($R_{S,20^\circ C}$)	7.1 Ω
Voltage U_{eff}	230 V
Peak intensity I_{max}	12 A
Number of pole pairs n_{pp}	1

We define the three phases as follows:

$$\begin{cases} I_U(\theta) = I_{max} \cos(n_{pp} \theta + \varphi) \\ I_V(\theta) = I_{max} \cos(n_{pp} \theta + \varphi - \frac{2\pi}{3}) \\ I_W(\theta) = I_{max} \cos(n_{pp} \theta + \varphi - \frac{4\pi}{3}) \end{cases} \quad (2.2)$$

Here, φ is the phase angle. The computational domain Ω consists of iron, air, permanent magnet and coils,

$$\Omega = \Omega_f \cup \Omega_{air} \cup \Omega_{mag} \cup \Omega_c \quad (2.3)$$

where we further subdivide the ferromagnetic and air subdomains into their rotor and stator parts,

$$\Omega_f = \Omega_{f,stat} \cup \Omega_{f,rot}, \quad \Omega_{air} = \Omega_{air,stat} \cup \Omega_{air,rot}. \quad (2.4)$$

Moreover, we subdivide the coil subdomains according to the distribution shown in Figure 2,

$$\Omega_c = \Omega_{U+} \cup \Omega_{U-} \cup \Omega_{V+} \cup \Omega_{V-} \cup \Omega_{W+} \cup \Omega_{W-}. \quad (2.5)$$

2.2 Partial differential equation

In the two-dimensional magnetostatic setting, the magnetic flux density $\mathbf{B} = \text{curl}((0, 0, u)^\top)$ for rotor position

$\theta \in [0, 2\pi]$ can be computed via the solution of the boundary value problem

$$\text{Find } u \in H_0^1(\Omega) : \int_{\Omega} v_{\theta}(x, |\nabla u|) \nabla u \cdot \nabla v dx = \int_{\Omega_c} j(\theta) v dx + \int_{\Omega_{mag}^{\theta}} R_{\theta} \begin{bmatrix} -M_y \\ M_x \end{bmatrix} \cdot \nabla v dx \quad (2.6)$$

for all $v \in H_0^1(\Omega)$, see e.g. [26].

Here, the magnetic reluctivity is a nonlinear function \hat{v} of the flux density $|\mathbf{B}| = |\nabla u|$ in the ferromagnetic subdomain and a constant $v_0 = 10^7 / (4\pi)$ elsewhere, i.e.,

$$v_{\theta}(x, |\nabla u|) = \begin{cases} \hat{v}(|\nabla u|) & x \in \Omega_f^{\theta} \\ v_0 & x \in \Omega_{air}^{\theta} \cup \Omega_c \cup \Omega_{mag}^{\theta} \end{cases} \quad (2.7)$$

with the rotated domains

$$\Omega_f^{\theta} = \Omega_{f,stat} \cup R_{\theta} \Omega_{f,rot} \quad (2.8)$$

$$\Omega_{air}^{\theta} = \Omega_{air,stat} \cup R_{\theta} \Omega_{air,rot} \quad (2.9)$$

$$\Omega_{mag}^{\theta} = R_{\theta} \Omega_{mag} \quad (2.10)$$

and R_{θ} a rotation matrix around angle θ ,

$$R_{\theta} = \begin{bmatrix} \cos \theta & -\sin \theta \\ \sin \theta & \cos \theta \end{bmatrix}. \quad (2.11)$$

The first term on the right hand side of (2.6) represents the impressed current density which is given by

$$j(x, \theta) = \chi_{\Omega_{U+}}(x) j_U(\theta) + \chi_{\Omega_{V+}}(x) j_V(\theta) + \chi_{\Omega_{W+}}(x) j_W(\theta) - \chi_{\Omega_{U-}}(x) j_U(\theta) - \chi_{\Omega_{V-}}(x) j_V(\theta) - \chi_{\Omega_{W-}}(x) j_W(\theta), \quad (2.12)$$

where χ_A denotes the characteristic function of a set A ,

$$\chi_A(x) = \begin{cases} 1 & x \in A, \\ 0 & \text{else.} \end{cases}$$

Here the current distribution is defined by :

$$j_p(\theta) = \frac{1}{S_{slot}} N_s I_p(\theta), \quad p \in \{U, V, W\} \quad (2.13)$$

with S_{slot} the cross-sectional area of one coil, N_s the number of turns per coil and I_U, I_V, I_W as defined in (2.2). The second term on the right hand side of (2.6) represents the magnetization $\mathbf{M} = (M_x, M_y)^T$ coming from permanent magnets which will be added in the course of the multi-material optimization procedure.

In the following, we will denote by u_{θ} the solution to the state equation (2.6).

We present here after the properties of interest of the materials (air, ferromagnetic, magnet) used in the machine.

Table 3: Material properties

Material	Reluctivity [$m.H^{-1}$]	Magnetization [$A.m^{-1}$]
Air	v_0	0
Copper	v_0	0
Ferromagnetic	$\hat{v}(\vec{B})$	0
Magnet	v_0	M_{max}

The maximum norm of the magnetization vector was chosen as $M_{max} = 2.33 \cdot 10^5 A.m^{-2}$ to fit data from [28] on ferrite magnets. The reluctivity of the magnets and of the copper coils is assimilated to the one of air to simplify further material interpolation and avoid complex schemes like the ones found in [37]. The non-linear behaviour of the ferromagnetic material is modelled with a Marrocco's BH curve approximation [24].

$$\hat{v}(|\vec{B}|) = \begin{cases} v_0 \left(\varepsilon + \frac{(c-\varepsilon)|\vec{B}|^{2\alpha}}{\tau + |\vec{B}|^{2\alpha}} \right) & \text{if } |\vec{B}| \leq B_{max}, \\ v_0 \left(1 - \frac{M_s}{|\vec{B}|} \right) & \text{else if } |\vec{B}| > B_s, \\ \exp \left(\frac{\gamma(|\vec{B}| - \beta)}{|\vec{B}|} \right) & \text{otherwise,} \end{cases} \quad (2.14)$$

where $B_s = \beta + \frac{\log(\frac{v_0}{\gamma})}{\gamma}$ and $M_s = B_s + \frac{1}{\gamma}$ and the coefficient of the Marrocco curve in Figure3 are defined in the Table 4.

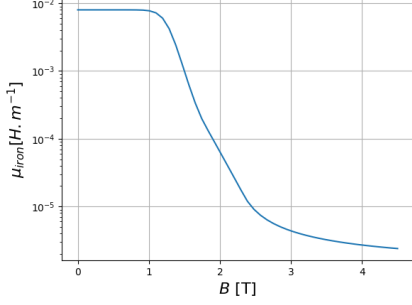
Table 4: Marrocco curve coefficient for the ferromagnetic material

Parameter	Value
α	6.84
β	$-1.30 \cdot 10^{-1}$
γ	4.86
ε	$1.57 \cdot 10^{-4}$
τ	$4.14 \cdot 10^3$
c	$1.90 \cdot 10^{-2}$
B_{max}	1.80 (T)

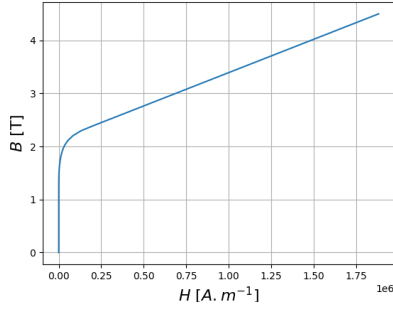
2.3 Torque computation method

For computing the torque, we chose a method based on Maxwell's stress tensor, Arkkio's method [30]. While co-energy torque computation methods were proven to be more precise and less prone to error, they are more costly in terms of computation time and not fit for optimization. Using Arkkio's method, the torque can be computed as

$$T = \frac{L_z v_0}{r_s - r_r} \int_S \sqrt{x^2 + y^2} B_r B_{\phi} dS \quad (2.15)$$



(a) Magnetic permeability



(b) Marrocco BH-curve

Figure 3: Non-linear characteristic for the ferromagnetic material.

where B_r and B_ϕ denote the radial and tangential magnetic induction, respectively, L_z denotes the length of the machine in z -direction and S denotes the surface between radii r_s and r_r in the air gap (with $r_s > r_r$).

In the setting of two-dimensional magnetostatics, the torque for the rotor position given by angle θ thus amounts to

$$T_\theta = T(u_\theta) = \frac{L_z v_0}{r_s - r_r} \int_S Q \nabla u_\theta \cdot \nabla u_\theta dS \quad (2.16)$$

$$\text{with } Q(x, y) = \begin{bmatrix} \frac{xy}{\sqrt{x^2+y^2}} & \frac{y^2-x^2}{2\sqrt{x^2+y^2}} \\ \frac{y^2-x^2}{2\sqrt{x^2+y^2}} & \frac{-xy}{\sqrt{x^2+y^2}} \end{bmatrix} \in \mathbb{R}^{2 \times 2}. \quad (2.17)$$

Determining the average torque by means of its instantaneous values can be very expensive. It is shown in [5] that a good approximation to the average torque can be obtained when evaluating the torque for only suitably chosen rotor positions,

$$\bar{T} = \frac{1}{4} \left(T_0 + T_{\frac{\pi}{12}} + T_{\frac{\pi}{6}} + T_{\frac{\pi}{4}} \right). \quad (2.18)$$

We compared the average torque obtained by evaluation at 500 equally distributed rotor positions between 0 and 2π with the value obtained by the four-point formula (2.18).

Table 5: Four static positions method error

Design	\bar{T} [N.m] (500 points)	\bar{T} [N.m] (4points)	Error [%]
Unbiased starting point*	$1.5790 \cdot 10^{-6}$	$5.7232 \cdot 10^{-6}$	262.4
Final design Table 7	1.1123	1.1129	0.048
Final design Table 9	1.4513	1.4516	0.027

* in this design $\rho_v = 0.5, \rho_{M_x} = 0.5, \rho_{M_y} = 0.5$ everywhere in the rotor

When the torque value is not equal to zero, the error found was to be lower than 0.1% as expected and described in literature [1]. This is solved beyond the first iteration.

3 Optimization problem

In this section, we define our optimization problem and reformulate the forward problem to fit the density-based topology optimization approach. Our goal is to maximize the average torque computed via (2.18),

$$(P_1) : \begin{cases} \text{maximize } \bar{T} = \frac{1}{4} \left(T(u_0) + T(u_{\frac{\pi}{12}}) + T(u_{\frac{\pi}{6}}) + T(u_{\frac{\pi}{4}}) \right) \\ \text{s.t. } u_\theta \text{ is a solution of (2.6) for } \theta \in \{0, \frac{\pi}{12}, \frac{\pi}{6}, \frac{\pi}{4}\} \end{cases} \quad (3.1)$$

This is achieved by finding the optimal material distribution consisting of ferromagnetic material, air and permanent magnets on the one hand, and the optimal magnetization direction of the permanent magnets on the other hand. Moreover, we will incorporate a bound on the maximum allowed permanent magnet volume.

3.1 Density based topology optimization

Let us reformulate the forward problem (2.6), introducing the three density variables respectively for the ferromagnetic material and the two components of the permanent magnets magnetization, $\rho_v, \rho_{M_x}, \rho_{M_y}$ defined in $\Omega_{rot}^\theta = R_\theta(\Omega_{f,rot} \cup \Omega_{air,rot} \cup \Omega_{mag})$. Moreover we introduce the rotated design variables

$$\begin{aligned} \rho_v^\theta(x, y) &= \rho_v(R_\theta((x, y)^\top)) \\ \rho_{M_x}^\theta(x, y) &= \rho_{M_x}(R_\theta((x, y)^\top)) \\ \rho_{M_y}^\theta(x, y) &= \rho_{M_y}(R_\theta((x, y)^\top)) \end{aligned}$$

which represent the design given by $\rho_v, \rho_{M_x}, \rho_{M_y}$ after rotation, and the vector of design variables $\mathbf{X} := [\rho_v, \rho_{M_x}, \rho_{M_y}]^\top$.

Given two interpolation functions

$$f_v : [0, 1] \rightarrow [0, 1], \quad f_M : [0, 1] \rightarrow [0, 1], \quad (3.2)$$

we define the operator

$$K_\theta : (\mathbf{X}, u, v) \mapsto \int_{\Omega} v(\rho_v^\theta, |\nabla u|) \nabla u \cdot \nabla v - \int_{\Omega_{rot}} f_v(1 - \rho_v^\theta) \frac{M_{max} f_M(|\vec{M}^\theta|)}{|\vec{M}^\theta|} R_\theta \begin{bmatrix} -M_y^\theta \\ M_x^\theta \end{bmatrix} \cdot \nabla v, \quad (3.3)$$

with the reluctivity function

$$v(\rho_v^\theta, |\nabla u|) = \begin{cases} \hat{v}(|\nabla u|) & \text{in } \Omega_{f,stat} \\ v_0 & \text{in } \Omega_c \cup \Omega_{air,stat} \\ v_0 + f_v(\rho_v^\theta)(\hat{v}(|\nabla u|) - v_0) & \text{in } \Omega_{rot} \end{cases} \quad (3.4)$$

and with the components of the magnetization vector $\vec{M}^\theta = (M_x^\theta, M_y^\theta)$ given in dependence of the two rotated density variables $\rho_{M_x}^\theta, \rho_{M_y}^\theta$,

$$(M_x^\theta, M_y^\theta) = \tilde{f}_{sd}(\rho_{M_x}^\theta, \rho_{M_y}^\theta) \quad (3.5)$$

for a mapping \tilde{f}_{sd} which will be discussed later on. Hence, the state equation (2.6) can be reformulated into

$$\begin{aligned} &\text{Find } u \in H_0^1(\Omega) : \\ &K_\theta(u, v, \mathbf{X}) = \int_{\Omega_c} j(\theta) v dx, \text{ for all } v \in H_0^1(\Omega). \end{aligned} \quad (3.6)$$

The optimization problem (P_1) can then be reformulated into

$$(P_2) : \begin{cases} \text{maximize } \bar{T} = \frac{1}{4} \sum_{\theta \in \{0, \frac{\pi}{12}, \frac{\pi}{6}, \frac{\pi}{4}\}} T(u_\theta) \\ \text{s.t. } u_\theta \text{ is a solution of the (3.6)} \quad \theta \in \{0, \frac{\pi}{12}, \frac{\pi}{6}, \frac{\pi}{4}\} \end{cases} \quad (3.7)$$

3.1.1 Material interpolation schemes

In density based topology optimization, the quality of the final solution is dependant on the choice of interpolation functions (equation (3.2)). We present here two existing schemes and a novel one based on properties of the topological derivative.

The polynomial interpolation scheme

$$f_n(\rho) = \rho^n \quad n > 0, \quad (3.8)$$

also referred to as SIMP (Solid Isotropic Material with Penalization), is the most used material interpolation scheme for topology optimization and allows for easy penalization of intermediate materials. However, it presents some symmetry issues and favors low ρ associated material in the final design. In [31], the authors compared this scheme to other schemes and concluded that the final design was not as good as many other proposed ones.

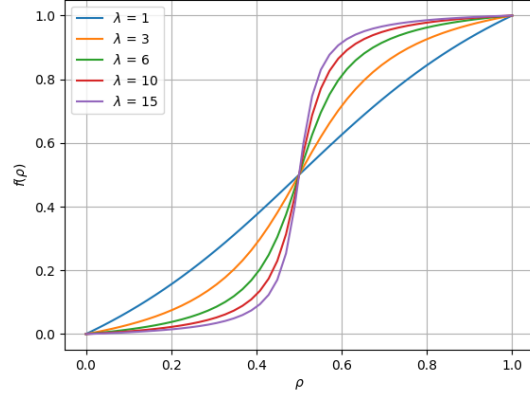


Figure 5: D. Lukàš's interpolation scheme

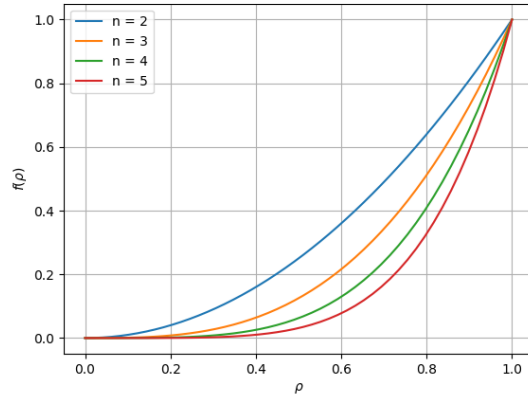


Figure 4: SIMP Polynomial interpolation scheme

To solve symmetry issues introduced by the classical polynomial interpolation, D. Lukàš introduced a new scheme in [21]:

$$f_\lambda(\rho) = \frac{1}{2} \left(1 + \frac{1}{\arctan(\lambda)} \arctan(\lambda(2\rho - 1)) \right), \quad \lambda > 0. \quad (3.9)$$

In this equation the particular invariant point $\rho = 0.5$ does not promote intermediate materials, grey material depends on λ values (cf. Figure 5).

High λ values permit to penalize intermediate materials but can lead to a poor convergence of the algorithm. A parameter study for λ led us to choose $\lambda = 5$. This interpolation method is chosen for the norm of the magnetization vector (f_M in (3.6)). Finally, we propose a new interpolation scheme as given in Figure 6, which is inspired by the topological derivative as done in [2], see also the the SIMP-All method for linear elasticity [9]. Here, we seek to design a material interpolation function whose derivative

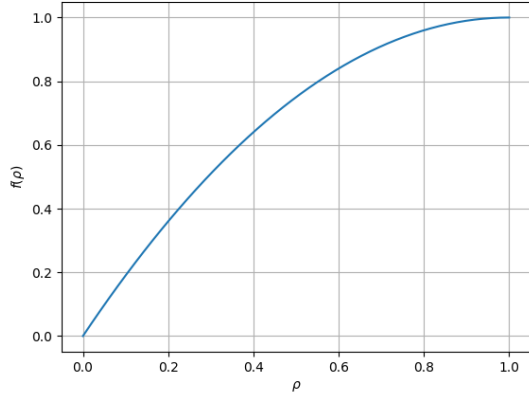


Figure 6: Topological derivative inspired interpolation scheme

with respect to the density variable ρ coincides with the topological derivative of the problem at $\rho = 0$ and $\rho = 1$. When interpolating between two linear materials with reluctivity values v_0 and v_1 , the conditions for the material interpolation function f according to [2] would read

$$\begin{cases} f(0) = 0, \\ f(1) = 1, \\ f'(0) = \frac{2v_0}{v_0+v_1}, \\ f'(1) = \frac{2v_1}{v_0+v_1}. \end{cases} \quad (3.10)$$

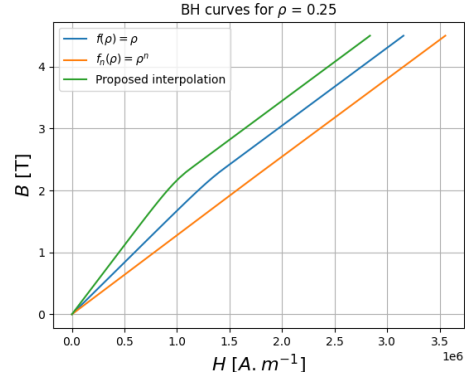
Due to the involved formula of the topological derivative for nonlinear magnetostatics [3], a mathematically rigorous extension of this method to the nonlinear setting is not straightforward. However, inspired by the particular behaviour of the Marrocco BH-curve where the magnetic reluctivity is almost constant for low flux density values, see Figure 3, we simply use this idea for that constant reluctivity value $v_1 := v_0 \varepsilon \approx 124.94$. Using cubic Hermite interpolation for the conditions (3.10), we obtain the polynomial

$$f(\rho) = \frac{2v_0}{v_0+v_1}\rho - \frac{v_0-v_1}{v_0+v_1}\rho^2. \quad (3.11)$$

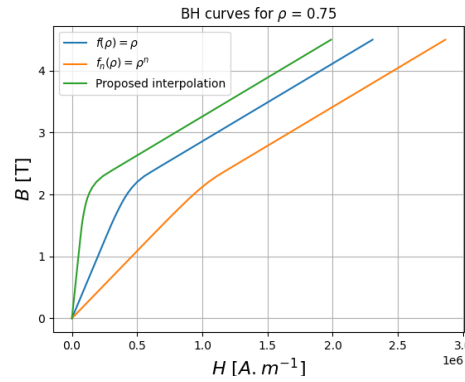
Note that the term of order 3 happens to vanish.

3.1.2 Magnetization vector transform

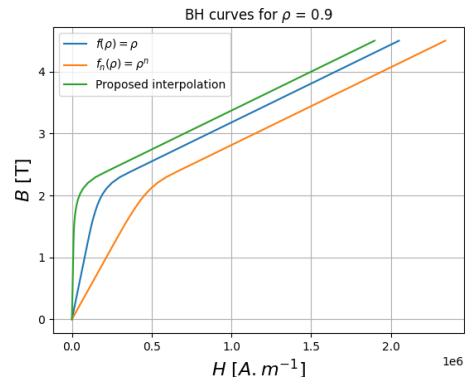
We deal with two magnetization density variables ρ_{M_x} and ρ_{M_y} in order to represent the magnetization direction (M_x, M_y) . One way of relating these quantities to each other would be to have ρ_{M_x} represent the first and ρ_{M_y} the second coordinate, resulting in a representation in Cartesian coordinates, which was also considered in [36]. In this case, however, some magnetization directions exhibit higher maximum magnetization than others, e.g.



(a) Interpolated BH curve for $\rho = 0.25$



(b) Interpolated BH curve for $\rho = 0.75$



(c) Interpolated BH curve for $\rho = 0.9$

Figure 7: Interpolated BH curves using material interpolation scheme (3.11).

where $\underline{w} = (w_0, w_{\frac{\pi}{12}}, w_{\frac{\pi}{6}}, w_{\frac{\pi}{4}})$ is a vector of Lagrange multipliers. The adjoint states λ_θ corresponding to problem (3.17) for different rotor positions θ are defined by $\frac{\partial \mathcal{L}}{\partial u_\theta}(\mathbf{X}, u_\theta, \lambda_\theta) = 0$, i.e. λ_θ is the solution to

$$\text{Find } \lambda_\theta \in H_0^1(\Omega) : \frac{\partial K_\theta}{\partial u}(\mathbf{X}, u_\theta, \lambda_\theta)(v) = -\frac{1}{4} \frac{\partial T}{\partial u}(u_\theta)(v) \quad (3.22)$$

$$\text{for all } v \in H_0^1(\Omega). \quad (3.23)$$

Here, the left and right hand side, respectively, involve the operators

$$\begin{aligned} \frac{d}{du} K_\theta(\mathbf{X}, u, \lambda)(v) &= \frac{d}{du} \left(\int_{\Omega} v(\rho_v^\theta, |\nabla u|) \nabla u \cdot \nabla \lambda \right)(v) \\ &= \int_{\Omega} v(\rho_v^\theta, |\nabla u|) \nabla v \cdot \nabla \lambda + \int_{\Omega} \frac{d}{du} v(\rho_v^\theta, |\nabla u|)(v) \nabla u \cdot \nabla \lambda \\ &= \int_{\Omega} v(\rho_v^\theta, |\nabla u|) \nabla v \cdot \nabla \lambda + \int_{\Omega} f_v(\rho_v^\theta) \frac{\hat{v}(|\nabla u|)}{|\nabla u|} (\nabla u \cdot \nabla v) (\nabla u \cdot \nabla \lambda) \\ \frac{d}{du} T(u)(v) &= 2 \frac{L_z v_0}{r_s - r_r} \int_S Q \nabla u \cdot \nabla v \, dS. \end{aligned} \quad (3.24)$$

Similarly to (3.18), we introduce the adjoint vector

$$\underline{\lambda} := (\lambda_0, \lambda_{\frac{\pi}{12}}, \lambda_{\frac{\pi}{6}}, \lambda_{\frac{\pi}{4}}). \quad (3.25)$$

Hence, the sensitivity associated with (3.21) amounts to

$$\begin{aligned} \frac{\partial \mathcal{L}}{\partial \mathbf{X}}(\mathbf{X}, \underline{u}, \underline{\lambda}) &= \sum_{\theta \in \{0, \frac{\pi}{12}, \frac{\pi}{6}, \frac{\pi}{4}\}} \frac{\partial K_\theta}{\partial \mathbf{X}}(\mathbf{X}, u_\theta, \lambda_\theta) \\ &+ \frac{\partial \psi(h_{v,f}(\mathbf{X}), \gamma_f, \mu)}{\partial \mathbf{X}} + \frac{\partial \psi(h_{v,mag}(\mathbf{X}), \gamma_{mag}, \mu)}{\partial \mathbf{X}} \end{aligned} \quad (3.26)$$

where we used that $\frac{\partial T}{\partial \mathbf{X}} = 0$ and $\frac{\partial j}{\partial \mathbf{X}} = 0$.

3.4 Update method

Several methods exist to consider the movement in electrical motors, such as the Moving Band (MB) technique described in [8]. Even when using high order elements in the MB, this method remains less accurate than the mortar element method [4]. A variant of the mortar method, the Nitsche method, is chosen to take into account the rotation [16]. The operator K_θ will be replaced by K_θ^{NM} and \mathcal{L} by \mathcal{L} to fit the new formulation (detailed in Appendix.A).

We introduce a triangular mesh with a total of N elements, with N_{rot} many elements inside the rotor domain Ω_{rot} . We use piecewise linear and globally continuous finite element basis functions to solve the state and adjoint equations and we represent the density variables $\rho_v, \rho_{M_x}, \rho_{M_y}$ as piecewise constant functions on the mesh corresponding to Ω_{rot} . Thus, these density variables can be represented by a vector of dimension N_{rot} consisting of the values of the discrete functions in each element. We will

use the same notation $\rho_v, \rho_{M_x}, \rho_{M_y}$ for the vectors representing the discretized density variables.

To comply with the bounds of the density variables, we introduce the projected gradient as defined in [27, p. 520]

$$\mathcal{G} := \left[\mathbf{P}_{\rho_v, [0,1]} \left(\frac{\partial \mathcal{L}}{\partial \rho_v} \right) \quad \mathbf{P}_{\rho_{M_x}, [0,1]} \left(\frac{\partial \mathcal{L}}{\partial \rho_{M_x}} \right) \quad \mathbf{P}_{\rho_{M_y}, [0,1]} \left(\frac{\partial \mathcal{L}}{\partial \rho_{M_y}} \right) \right]^\top, \quad (3.27)$$

with the projection operator $\mathbf{P}_{\rho, [a,b]} : \mathbb{R}^{N_{rot}} \rightarrow \mathbb{R}^{N_{rot}}$ defined by

$$\left(\mathbf{P}_{\rho, [a,b]}(X) \right)_i = \begin{cases} X_i & \text{if } \rho_i \in]a, b[, \\ \min(0, X_i) & \text{if } \rho_i = a, \\ \max(0, X_i) & \text{if } \rho_i = b, \end{cases} \quad (3.28)$$

for $i = 1, \dots, N_{rot}$. This in itself allows for finer geometry to emerge by amplifying the relative importance of the gradient where change in the density function can be made.

From the sensitivity we derive the update equation at iteration n

$$\mathbf{X}_i^{n+1} = Q_{[0,1]} \left(\mathbf{X}_i^n - s \frac{\mathcal{G}_i}{|\mathcal{G}_i|} \right), \quad \text{for } i = 1, \dots, N_{rot} \quad (3.29)$$

with the projection operator $Q_{[a,b]} : \mathbb{R}^{3N_{rot}} \rightarrow \mathbb{R}^{3N_{rot}}$ defined by

$$\left(Q_{[a,b]}(\mathbf{v}) \right)_i = \max(a, \min(b, v_i)) \quad (3.30)$$

for a vector $\mathbf{v} = (v_1, \dots, v_{N_{rot}})^\top \in \mathbb{R}^{3N_{rot}}$ and $i = 1, \dots, N_{rot}$, to enforce the bounds of the density variables. Here, s denotes the step size which is chosen in such a way that a descent of the augmented Lagrangian is obtained,

$$L(\mathbf{X}^{n+1}, \underline{u}^{n+1}) < L(\mathbf{X}^n, \underline{u}^n) \quad (3.31)$$

with \underline{u}^n is the vector of states for the design represented by \mathbf{X}^n .

3.5 Filtering and projection method

In density-based topology optimization, checkerboard patterns and small isolated elements of one material are avoided using filtering methods at each step of gradient descent. While this filtering has a regularizing effect on the density variables, it may introduce more gray areas. Therefore, in the next step, so-called projection methods are applied in order to get a more defined shape. This combination allows achieving smoother and more defined boundaries between the materials in the final design.

In our approach, in the first step we perform density filtering by solving the PDE

$$-r^2 \nabla^2 \rho + \rho = \rho_{ref} \quad r > 0. \quad (3.32)$$

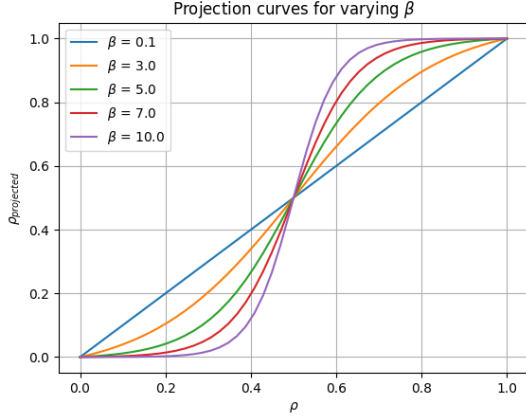


Figure 9: Comparison of projection curves for a varying β parameter.

with ρ_{ref} the given density function, which is commonly referred to as Helmholtz filtering [19]. This mesh-independency filter modifies the sensitivity by averaging on the neighbor cells. The parameter r is the radius of influence of the filtering and is defined in our case as a factor δ of the minimum representative mesh-element length h , i.e. $r = \delta h$.

For the projection step, we choose the function proposed in [35],

$$f_{\rho_{cut},\beta}(\rho) = \frac{\tanh(\beta(\rho - \rho_{cut})) + \tanh(\beta\rho_{cut})}{\tanh(\beta(1 - \rho_{cut})) + \tanh(\beta\rho_{cut})} \quad (3.33)$$

$\rho_{cut} \in [0, 1]; \beta > 0$

with $\rho_{cut} = 0.5$ such as not to favor one material. The other parameters δ and β are chosen to preserve the equilibrium between the two parts of the filtering step.

We applied the filtering technique (3.32) and the projection technique (3.33) for the material densities. The same PDE-based filter (3.32) is applied for the densities ρ_{M_x} and ρ_{M_y} , to favor uniform magnetization direction in a magnet area while the projection (3.33) is only applied on $|\vec{M}|$ to avoid scaling issues.

3.6 Direct penalization of intermediate materials

Some final designs can still present fuzzy boundaries and intermediate material, especially if the optimization starting point is near a local minimum. To help overcome this issue, we propose to penalize the intermediate materials directly as done in the phase-field topology optimization method [13] and add to the cost function the following

term with a weight $\gamma > 0$:

$$I_\gamma(\rho) = \frac{4\gamma}{V_{\Omega_{rot}}} \int_{\Omega_{rot}} \rho(x)(1 - \rho(x))dx. \quad (3.34)$$

The penalization is only applied on iron density ρ_v and the magnetization norm $|\vec{M}|$.

3.7 Post-processing: K-mean heuristic

In our optimization problem we look for permanent magnetization directions which may change continuously in space. In order to obtain designs which comply with feasibility constraints, we here propose a post-processing step. A K-mean heuristic [22] clustering method is applied. Here, we suggest adapting it to create clusters of elements of similar magnetization direction.

Let us define a point $P = (p_x, p_y, p_{\beta_M})$ by its coordinates p_x, p_y in the 2D plane and its magnetization angle p_{β_M} . We define a set of k points C_1, \dots, C_k where $C_j = (c_{x,j}, c_{y,j}, -)$, which we will refer to as centroids, and which are first randomly sampled in the 2D plane.

Let $P_1, \dots, P_{N_{rot}}$ be the centroids of the triangles in the rotor domain Ω_{rot} . At each step of the algorithm, we associate each point P_i with the closest centroid $C_j \in S_k$ using a modified 3D Euclidean distance d_α . For two such points $P_i = (p_{x,i}, p_{y,i}, p_{\beta_{M,i}})$ and $C_j = (c_{x,j}, c_{y,j}, c_{\beta_{M,j}})$, this modified distance function is defined as

$$d_\alpha : \mathbb{R}^3 \times \mathbb{R}^3 \rightarrow \mathbb{R}$$

$$(P_i, C_j) \mapsto \sqrt{\left(\frac{p_{x,i} - c_{x,j}}{N_x}\right)^2 + \left(\frac{p_{y,i} - c_{y,j}}{N_y}\right)^2 + \alpha \left(\frac{p_{\beta_{M,i}} - c_{\beta_{M,j}}}{2\pi}\right)^2} \quad (3.35)$$

where N_x, N_y, α are three weighting constants which can be used to tune the method.

By this procedure, we get k point clusters S_1, \dots, S_k with $S_j = \{P_i : d_\alpha(P_i, C_j) < d_\alpha(P_i, C_l) \text{ for all } l \neq j\}$ for $j = 1, \dots, k$. Thus, all points in cluster S_j are closer to point C_j in terms of d_α than to any other centroid C_l .

The positions of the centroids C_1, \dots, C_k are then updated according to the mean coordinates of the points associated with them,

$$C_j \leftarrow (\mu_{x,j}, \mu_{y,j}, \mu_{\beta_{M,j}}) \text{ where } \mu_{x,j} = \frac{1}{\#S_j} \sum_{P_i \in S_j} p_{x,i} \quad (3.36)$$

and $\mu_{y,j}, \mu_{\beta_{M,j}}$ defined analogously. Here, $\#S_j$ denotes the cardinality of S_j . In the first iteration where $c_{\beta_{M,j}}$ is not defined, we use the modified 2D Euclidean distance $d_{\alpha=0}$.

4 Application to the magnetostatics problem

All computations were conducted using the NGSolve [12, 32] framework with its python interface. Three sets of results are presented in this section to validate the proposed

strategy. For the different optimization sets, the starting points are given in Table 6.

The first design in Table 6 is used for the Iron-Air optimization. The results for the material distribution are given in Table 7 for different volume fractions $f_{v,f}$. These results are coherent with the literature of synchro-reluctant actuators with distributed winding [34], with a phase angle $\varphi = \frac{5\pi}{6}$ and one pair of poles. This phase angle corresponds to the maximum torque of the machine. Results can also be compared with results found in [11, 25] which are validated by means of *JMAG*.

For the multi-material topology optimization including magnets, the final design obtained at 40% of ferromagnetic material is used as a starting point. Results for magnets distribution are presented in Table 8. As expected, magnets are distributed on the air barriers domain. Several constraints on magnets volume were chosen. One should note that the ferromagnetic distribution is modified at the outer radius of the rotor. Without magnets, the reluctance torque is equal to 1.0768 [N.m]. Optimized torque and post-processed values after k-mean clustering are given, the number of clusters is fixed to $k = 5$.

In order to validate the proposed strategy, a new phase angle is chosen. It is equal to $\varphi = \frac{3\pi}{32}$. The objective is to find the optimal materials distribution to maximize the torque at this phase angle. An unbiased starting point is chosen, where homogeneous grey materials are set in the rotor such as $\rho_v = 0.5, \rho_{M_x} = 0.5, \rho_{M_y} = 0.5$. The optimal rotor structure is given in Table 9. Again, we present optimized torques as well as the torque values after post-processing, where we used $k = 5$ clusters for the K-mean clustering. Results on the torque value are comparable for the previously obtained but at higher magnets volume, which is also coherent with literature. On the other hand, the first optimal multi-material model has larger reluctant torque due to optimal current supply in the q-axis.

5 Conclusion and outlooks

In this study we proposed a novel multi-material interpolation method to determine the optimal distribution of air, iron, and magnets for PMSynRM. The interpolation takes into account magnetization amplitudes and direction, and a post-processing clustering method is also suggested to homogenize magnets direction for feasibility constraints. This study also investigated the use of the four statics positions method to reduce global computation time. With further work, an exhaustive comparison with other interpolation schemes will be considered, and the extension to multiobjective optimization under gradient-based methods.

A Nitsche-mortaring reformulation

Several methods exist to consider the movement in electrical motors, such as the Moving Band (MB) technique described in [8], even when using high order elements in the MB, this method remains less accurate than the mortar element method [4]. A variant of the mortar method, the Nitsche method, is chosen to take into account the rotation [16]. Let us define the adapted operator K_θ^{NM} to fit the new formulation

$$\begin{aligned} K_\theta^{NM}(\mathbf{X}, u, \eta, v, \mu) = & \sum_{i \in \{\text{rot}, \text{stat}\}} \left(\int_{\Omega_i} v(\rho_v^\theta, |\nabla u_i|) \nabla u_i \cdot \nabla v_i \right) \\ & - \int_{\Omega_{\text{rot}}} f_v(1 - \rho_v^\theta) \frac{M_{\max} f_M(|\vec{M}|)}{|\vec{M}|} R_\theta \begin{bmatrix} -M_y^\theta \\ M_x^\theta \end{bmatrix} \cdot \nabla v_{\text{rot}} \\ & + \sum_{i \in \{\text{rot}, \text{stat}\}} \left(- \int_{\partial\Omega_i} v_0 \frac{\partial u_i}{\partial n} (v_i - \mu) - \int_{\partial\Omega_i} v_0 \frac{\partial v_i}{\partial n} (u_i - \eta) \right) \\ & + \frac{\alpha p^2}{h} \int_{\partial\Omega_i} (u_i - \eta)(v_i - \mu), \end{aligned} \quad (\text{A.1})$$

where $(u, \eta, v, \mu) \in V \times W \times V \times W$ and V, W are defined as

$$\begin{cases} V = \{v = (v_{\text{rot}}, v_{\text{stat}}) \in H^1(\Omega_{\text{rot}}) \times H^1(\Omega_{\text{stat}}), v = 0 \text{ on } \partial\Omega\}, \\ W = \{w \in L^2(\partial\Omega_{\text{rot}} \cap \partial\Omega_{\text{stat}})\}. \end{cases} \quad (\text{A.2})$$

Here, $\alpha > 0$ is a stabilization parameter which we chose as $\alpha = 160$, $p = 1$ denotes the polynomial degree of the finite element discretization and h the diameter of the largest element of the mesh. Moreover, recall the implicit dependence of $\vec{M} = (M_x^\theta, M_y^\theta)^\top$ on the density variables $\rho_{M_x^\theta}, \rho_{M_y^\theta}$ (3.5), (3.14).

Hence the state equation (3.6) can be formulated as

$$\text{Find } (u_\theta, \eta_\theta) \in V \times W, K_\theta^{NM}(\mathbf{X}_p, u_\theta, \eta_\theta, v, \mu) = \int_{\Omega_{\text{stat}}} j(\theta) v dx \quad \text{for all } (v, \mu) \in V \times W. \quad (\text{A.3})$$

In a similar manner, the adjoint equation (3.22) can be re-

Table 6: Starting designs

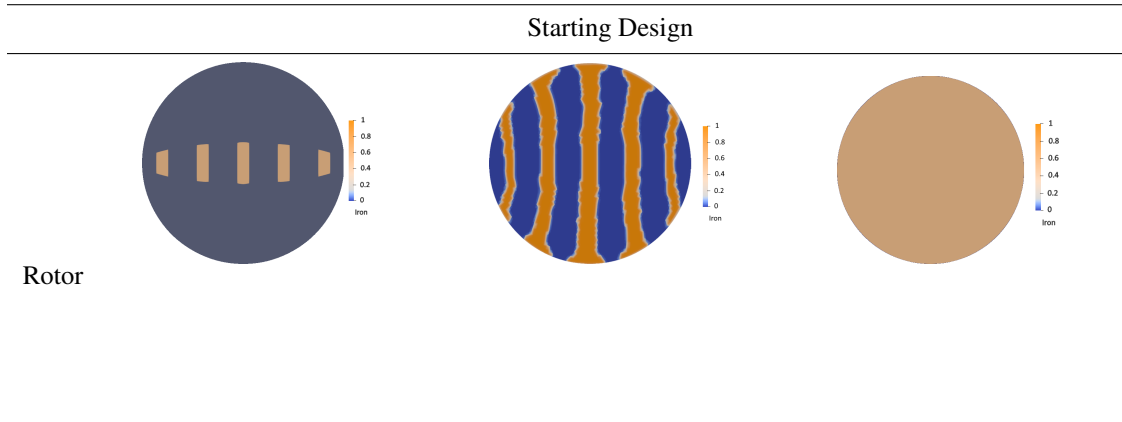


Table 7: Designs Iron-Air

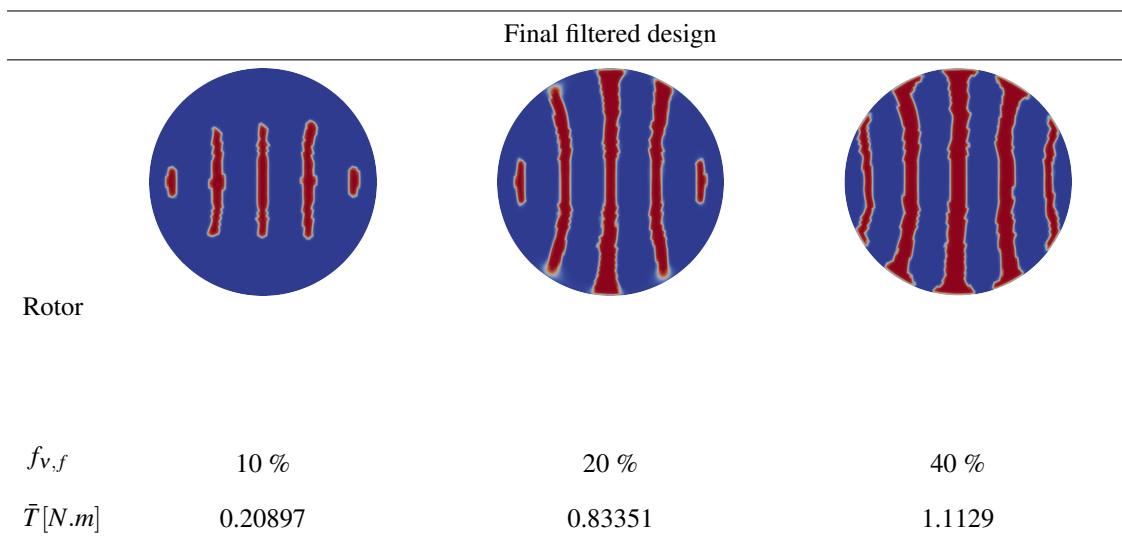


Table 8: Designs Magnet-Air-Iron

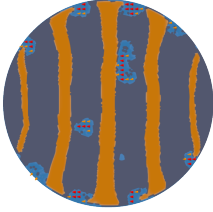
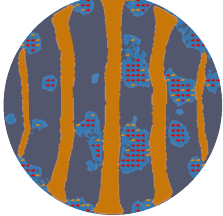
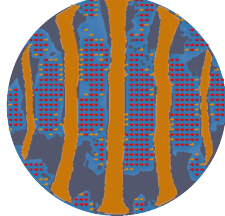
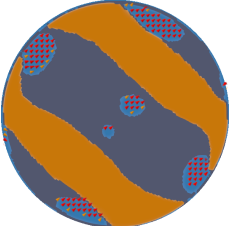
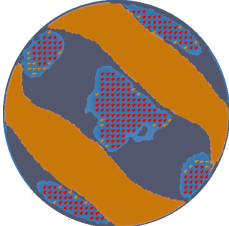
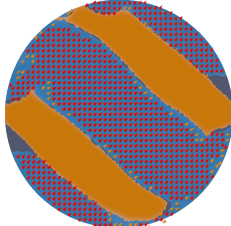
Final filtered designs			
			
Rotor			
$f_{v,mag}$	7.5 %	15 %	30 %
$\bar{T} [N.m]$	1.2830	1.4729	1.9000
$\bar{T}_{Kmeans} [N.m]$	1.2646	1.4469	1.8671

Table 9: Designs Iron-Air-Magnets

Final Design			
			
Rotor			
$f_{v,mag}$	10%	20%	Not bounded
$\bar{T} [N.m]$	1.2710	1.4513	2.0484
$\bar{T}_{Kmeans} [N.m]$	1.1097	1.3863	1.6422

defined as

$$\text{Find } (w_\theta, \mu_\theta) \in V \times W : \frac{\partial K_\theta^{NM}}{\partial (u, \eta)}(\mathbf{X}, u_\theta, \eta_\theta, w_\theta, \mu_\theta)(\hat{u}, \hat{\eta}) = -\frac{1}{4} \frac{\partial T}{\partial u}(u_\theta)(\hat{u}) \quad (\text{A.4})$$

for all $(\hat{u}, \hat{\eta}) \in V \times W$ for each $\theta \in \{0, \frac{\pi}{12}, \frac{\pi}{6}, \frac{\pi}{4}\}$.

The corresponding Lagrangian reads

$$\mathcal{L}(\mathbf{X}, \underline{u}, \underline{\eta}, \underline{v}, \underline{\mu}) := L(\mathbf{X}, \underline{u}) + \sum_{\theta \in \{0, \frac{\pi}{12}, \frac{\pi}{6}, \frac{\pi}{4}\}} K_\theta^{NM}(\mathbf{X}, u_\theta, \eta_\theta, v_\theta, \mu_\theta) - \int_{\Omega_{\text{rot}}} j(\theta) v_\theta, \quad (\text{A.5})$$

and its gradient is given by

$$\frac{\partial \mathcal{L}}{\partial \mathbf{X}}(\mathbf{X}, \underline{u}, \underline{\eta}, \underline{v}, \underline{\mu}) = \left(\sum_{\theta \in \{0, \frac{\pi}{12}, \frac{\pi}{6}, \frac{\pi}{4}\}} \frac{\partial K_\theta^{NM}}{\partial \mathbf{X}}(\mathbf{X}, u_\theta, \eta_\theta, v_\theta, \mu_\theta) - \frac{1}{4} \frac{\partial T_\theta}{\partial \mathbf{X}} \right) + \frac{\partial \psi(h_{v,f}(\mathbf{X}), \gamma_f, \mu)}{\partial \mathbf{X}} + \frac{\partial \psi(h_{v,mag}(\mathbf{X}), \gamma_{mag}, \mu)}{\partial \mathbf{X}}. \quad (\text{A.6})$$

References

- [1] P. Akiki, M. Hage-Hassan, M. Bensetti, J.-C. Vanier, D. Prieto, and M. McClelland. Axial ferrite-magnet-assisted synchronous reluctance motor. In *2018 XIII International Conference on Electrical Machines (ICEM)*, pages 583–589, 2018.
- [2] S. Amstutz, C. Dapogny, and À. Ferrer. A consistent relaxation of optimal design problems for coupling shape and topological derivatives. *Numerische Mathematik*, 140(1):35–94, 3 2018.
- [3] S. Amstutz and P. Gangl. Topological derivative for the nonlinear magnetostatic problem. *Electron. Trans. Numer. Anal.*, 51:169–218, 2019.
- [4] O. Antunes, J. Bastos, N. Sadowski, A. Razek, L. Santandrea, F. Bouillault, and F. Rapetti. Using hierarchic interpolation with mortar element method for electrical machines analysis. *IEEE Transactions on Magnetics*, 41(5):1472–1475, 2005.
- [5] N. Bianchi, L. Alberti, M. Popescu, and T. Miller. MMF Harmonics Effect on the Embedded FE-Analytical Computation of PM Motors. In *Conference Record - IAS Annual Meeting (IEEE Industry Applications Society)*, pages 1544 – 1551, 2007.
- [6] J. S. Choi and J. Yoo. Optimal design method for magnetization directions of a permanent magnet array. *Journal of Magnetism and Magnetic Materials*, 322(15):2145–2151, 2010.
- [7] J. S. Choi, J. Yoo, S. Nishiwaki, and K. Izui. Optimization of Magnetization Directions in a 3-D Magnetic Structure. *IEEE Transactions on Magnetics*, 46(6):1603–1606, 2010.
- [8] B. Davat, Z. Ren, and M. Lajoie-Mazenc. The movement in field modeling. *IEEE Transactions on Magnetics*, 21(6):2296–2298, 1985.
- [9] A. Ferrer. Simp-all: A generalized simp method based on the topological derivative concept. *International Journal for Numerical Methods in Engineering*, 120(3):361–381, 2019.
- [10] C. Fong. Analytical methods for squaring the disc, 2019.
- [11] P. Gangl, S. Köthe, C. Mellak, A. Cesarano, and A. Mütze. Multi-objective free-form shape optimization of a synchronous reluctance machine. *arXiv:2010.10117 [cs, math]*, 10 2020. arXiv: 2010.10117.
- [12] P. Gangl, K. Sturm, M. Neunteufel, and J. Schöberl. Fully and Semi-Automated Shape Differentiation in NGSolve. *arXiv:2004.06783 [math]*, 10 2020. arXiv: 2004.06783.
- [13] H. Garcke, C. Hecht, M. Hinze, and C. Kahle. Numerical Approximation of Phase Field Based Shape and Topology Optimization for Fluids. *SIAM J. Sci. Comput.*, 37(4):A1846–A1871, 1 2015.
- [14] F. Guo, M. Salameh, M. Krishnamurthy, and I. P. Brown. Multimaterial Magneto-Structural Topology Optimization of Wound Field Synchronous Machine Rotors. *IEEE Transactions on Industry Applications*, 56(4):3656–3667, 2020.
- [15] H. Heidari, A. Rassölkin, A. Kallaste, T. Vaimann, E. Andriushchenko, A. Belahcen, and D. V. Lukichev. A Review of Synchronous Reluctance Motor-Drive Advancements. *Sustainability*, 13(2):729, 1 2021.
- [16] K. Hollaus, D. Feldengut, J. Schoeberl, M. Wabro, and D. Omeragic. Nitsche-type Mortaring for Maxwell’s Equations. *PIERS 2010 Cambridge - Progress in Electromagnetics Research Symposium, Proceedings*, 2010.
- [17] T. Ishikawa, P. Xie, and N. Kurita. Topology Optimization of Rotor Structure in Permanent Magnet Synchronous Motors Considering Ease of Manufacturing. *IEEJ Journal IA*, 4(4):469–475, 2015.
- [18] J. Kim, K. H. Sun, W. Kim, and J. E. Kim. Magnetic torque maximization in a camera shutter module by the topology optimization. *J Mech Sci Technol*, 24(12):2511–2517, 12 2010.

- [19] B. S. Lazarov and O. Sigmund. Filters in topology optimization based on Helmholtz-type differential equations. *Int. J. Numer. Meth. Engng.*, 86(6):765–781, 5 2011.
- [20] J. Lee, E. M. Dede, and T. Nomura. Simultaneous Design Optimization of Permanent Magnet, Coils, and Ferromagnetic Material in Actuators. *IEEE Transactions on Magnetics*, 47(12):4712–4716, 2011.
- [21] D. Lukáš. An Integration of Optimal Topology and Shape Design for Magnetostatics. In A. M. Anile, G. Alì, and G. Mascali, editors, *Scientific Computing in Electrical Engineering*, pages 227–232, Berlin, Heidelberg, 2006. Springer Berlin Heidelberg.
- [22] J. MacQueen and others. Some methods for classification and analysis of multivariate observations. In *Proceedings of the fifth Berkeley symposium on mathematical statistics and probability*, volume 1, pages 281–297. Oakland, CA, USA, 1967. Issue: 14.
- [23] S. S. Maroufian and P. Pillay. PM assisted synchronous reluctance machine design using AlNiCo magnets. In *2017 IEEE International Electric Machines and Drives Conference (IEMDC)*, pages 1–6, Miami, FL, USA, 5 2017. IEEE.
- [24] A. Marrocco. Analyse numérique de problèmes d'électrotechnique. *Ann. Sc. Math. Québec*, 1(2):271–296, 1977.
- [25] C. Mellak, K. Krischan, and A. Muetze. Synchronous Reluctance Machines as Drives for Rotary Anode X-Ray Tubes-A Feasibility Study. In *2018 XIII International Conference on Electrical Machines (ICEM)*, pages 2613–2618, Alexandroupoli, 9 2018. IEEE.
- [26] P. Monk and others. *Finite element methods for Maxwell's equations*. Oxford University Press, 2003.
- [27] J. Nocedal and S. J. Wright, editors. *Penalty, Barrier, and Augmented Lagrangian Methods*, pages 488–525. Springer New York, New York, NY, 1999.
- [28] A. S. Nunes, L. Daniel, M. Hage-Hassan, and M. Domenjoud. Modeling of the magnetic behavior of permanent magnets including ageing effects. *Journal of Magnetism and Magnetic Materials*, 512:166930, 10 2020.
- [29] M. Risticvic, D. Iles, and A. Moeckel. Design of an interior permanent magnet synchronous motor supported by the topology optimization algorithm. In *2016 International Symposium on Power Electronics, Electrical Drives, Automation and Motion (SPEEDAM)*, pages 221–225, Capri, Italy, 6 2016. IEEE.
- [30] N. Sadowski, Y. Lefevre, M. Lajoie-Mazenc, and J. Cros. Finite element torque calculation in electrical machines while considering the movement. *IEEE Trans. Magn.*, 28(2):1410–1413, 3 1992.
- [31] S. Sanogo and F. Messine. Topology optimization in electromagnetism using SIMP method: Issues of material interpolation schemes. *COMPEL*, 37(6):2138–2157, 11 2018.
- [32] J. Schöberl. C++11 Implementation of Finite Elements in NGSolve. Technical report, Institute for Analysis and Scientific Computing, 9 2014.
- [33] O. Sigmund. A 99 line topology optimization code written in Matlab. *Structural and Multidisciplinary Optimization*, 21, 2001.
- [34] A. Vagati, G. Franceschini, I. Marongiu, and G. Troglia. Design criteria of high performance synchronous reluctance motors. In *Conference Record of the 1992 IEEE Industry Applications Society Annual Meeting*, pages 66–73 vol.1, 1992.
- [35] F. Wang, B. S. Lazarov, and O. Sigmund. On projection methods, convergence and robust formulations in topology optimization. *Structural and Multidisciplinary Optimization*, 43(6):767–784, 6 2011.
- [36] S. Wang, D. Youn, H. Moon, and J. Kang. Topology optimization of electromagnetic systems considering magnetization direction. *Magnetics, IEEE Transactions on*, 41:1808 – 1811, 2005.
- [37] W. Zuo and K. Saitou. Multi-material topology optimization using ordered SIMP interpolation. *Struct Multidisc Optim*, 55(2):477–491, 2 2017.

Erschienenene Preprints ab Nummer 2020/1

- 2020/1 D. Pacheco, T. Müller, O. Steinbach, G. Brenn: A mixed finite element formulation for generalised Newtonian fluid flows with appropriate natural outflow boundary conditions
- 2020/2 U. Langer, O. Steinbach, F. Tröltzsch, H. Yang: Unstructured space-time finite element methods for optimal sparse control of parabolic equations
- 2020/3 D.R.Q. Pacheco, R. Schussnig, O. Steinbach, T.-P. Fries: A fully consistent equal-order finite element method for incompressible flow problems
- 2020/4 U. Langer, O. Steinbach, F. Tröltzsch, H. Yang: Unstructured space-time finite element methods for optimal control of parabolic equations
- 2020/5 P. Gangl, K. Sturm, M. Neunteufel, J. Schöberl: Fully and Semi-Automated Shape Differentiation in NGSolve
- 2020/6 U. Langer, O. Steinbach, F. Tröltzsch, H. Yang: Space-time finite element discretization of parabolic optimal control problems with energy regularization
- 2020/7 G. Of, R. Watschinger: Complexity analysis of a fast directional matrix-vector multiplication
- 2020/8 P. Gangl, K. Sturm: Topological derivative for PDEs on surfaces
- 2020/9 D. R. Q. Pacheco, O. Steinbach: A continuous finite element framework for the pressure Poisson equation allowing non-Newtonian and compressible flow behaviour
- 2020/10 S. Kurz, S. Schöps, G. Unger, F. Wolf: Solving Maxwell's Eigenvalue Problem via Isogeometric Boundary Elements and a Contour Integral Method
- 2020/11 U. Langer, M. Schanz, O. Steinbach, W. L. Wendland (eds.): 18th Workshop on Fast Boundary Element Methods in Industrial Applications , Book of Abstracts
- 2020/12 P. Gangl, S. Köthe, C. Mellak, A. Cesarano, A. Mütze: Multi-objective free-form shape optimization of a synchronous reluctance machine
- 2021/1 O. Steinbach, M. Zank: A generalized inf-sup stable variational formulation for the wave equation
- 2021/2 U. Langer, O. Steinbach, H. Yang: Robust discretization and solvers for elliptic optimal control problems with energy regularization
- 2021/3 R. Löscher, O. Steinbach, M. Zank: Numerical results for an unconditionally stable space-time finite element method for the wave equation
- 2021/4 O. Steinbach, P. Gaulhofer: On space-time finite element domain decomposition methods for the heat equation
- 2021/5 D. R. Q. Pacheco, O. Steinbach: Space-time finite element tearing and interconnecting domain decomposition methods
- 2021/6 U. Langer, O. Steinbach, F. Tröltzsch, H. Yang: Space-time finite element methods for the initial temperature reconstruction
- 2021/7 J. Zapletal, R. Watschinger, G. Of, M. Merta: Semi-analytic integration for a parallel space-time boundary element method modeling the heat equation
- 2021/8 R. Watschinger, G. Of: An integration by parts formula for the bilinear form of the hypersingular boundary integral operator for the transient heat equation in three spatial dimensions
- 2021/9 O. Steinbach, C. Urzua-Torres: A new approach to space-time boundary integral equations for the wave equation
- 2021/10 O. Steinbach, C. Urzua-Torres, M. Zank: Towards coercive boundary element methods for the wave equation
- 2021/11 R. Watschinger, M. Merta, G. Of, J. Zapletal: A parallel fast multipole method for a space-time boundary element method for the heat equation